Electrode displacement strain imaging of thermally-ablated liver tissue in an *in vivo* animal model

N. Rubert
Department of Medical Physics, University of Wisconsin-Madison, 1111 Highland Avenue, Madison, Wisconsin 53706

S. Bharat
Department of Medical Physics, University of Wisconsin-Madison, 1111 Highland Avenue, Madison, Wisconsin 53706 and Department of Electrical and Computer Engineering, University of Wisconsin-Madison, 1415 Engineering Drive, Madison, Wisconsin 53706

R. J. DeWall
Department of Biomedical Engineering, University of Wisconsin-Madison, 1550 Engineering Drive, Madison, Wisconsin 53706

A. Andreano and C. Brace
Department of Radiology, University of Wisconsin-Madison, University of Wisconsin-Madison, 1111 Highland Avenue, Madison, Wisconsin 53706

J. Jiang
Department of Medical Physics, University of Wisconsin-Madison, 1111 Highland Avenue, Madison, Wisconsin 53706

L. Sampson
Department of Radiology, University of Wisconsin-Madison, 1111 Highland Avenue, Madison, Wisconsin 53706

T. Varghese[a]
Department of Medical Physics, University of Wisconsin-Madison, 1111 Highland Avenue, Madison, Wisconsin 53706; Department of Electrical and Computer Engineering, University of Wisconsin-Madison, 1415 Engineering Drive, Madison, Wisconsin 53706; and Department of Biomedical Engineering, University of Wisconsin-Madison, 1550 Engineering Drive, Madison, Wisconsin 53706

Purpose: Percutaneous thermal ablation is increasingly being used to destroy hepatic tumors *in situ*. The success of ablative techniques is highly dependent on adequate ablation zone monitoring, and ultrasound-based strain imaging could become a convenient and cost-effective means to delineate ablation zone boundaries. This study investigates *in vivo* electrode displacement-based strain imaging for monitoring hepatic ablation procedures that are difficult to perform with conventional elastography.
Methods: In our method, minute displacements (less than a millimeter) are applied to the unconstrained end of the ablation electrode, resulting in localized tissue deformation within the ablation zone that provides the mechanical stimuli required for strain imaging. This article presents electrode displacement strain images of radiofrequency ablation zones created in porcine liver *in vivo* ($n=13$).
Results: Cross-sectional area measurements from strain images of these ablation zones were obtained using manual and automated segmentation. Area measurements from strain images were highly correlated with areas measured on histopathology images, quantitated using linear regression ($R=0.894$, $P<0.001$ and $R=0.828$, $P<0.001$, respectively).
Conclusions: This study further demonstrates that electrode displacement elastography is capable of providing high-contrast images using widely available commercial ultrasound systems which may potentially be used to assess the extent of thermal ablation zones. © *2010 American Association of Physicists in Medicine*. [DOI: 10.1118/1.3301603]

I. INTRODUCTION

Based on data compiled by the National Center for Health Statistics between 1960 and 2004, the mortality rate due to liver cancer has been steadily increasing over the past two decades.[1] Surgical resection offers treatment for some patients, but in many patients afflicted with hepatic tumors,

poor liver function and/or distribution of the tumors may prevent its use.[2] An alternative to surgical resection, percutaneous thermal ablation can be used to destroy the tumor *in situ*, and is evolving into one of the more popular minimally invasive treatments for hepatic tumors. Several methods are available for delivering the thermal energy to the target tumor,[3–5] with radiofrequency (RF) ablation being the most popular choice worldwide.

When performing RF ablation, an electrode is placed into the area of tissue to be ablated for localized thermal therapy. Ionic agitation in the tissue adjacent to the electrically active region of the electrode causes intense localized heating, leading to instant tissue necrosis for ablation temperatures greater than 60 °C.[6,7]

Paramount to the success of any thermal ablation technique is that the treatment completely destroy all viable tumor tissue and an adequate margin surrounding the tumor. The margin is to ensure that any microscopic invasions around the periphery of the tumor have been destroyed, in order to prevent tumor regrowth.[8] Thus, for minimally invasive therapies such as RF ablation, it is crucial that medical personnel have access to imaging modalities that accurately portray the extent of the ablation zone.

Ultrasound has been widely utilized for guiding electrode placement for RF or microwave ablation procedures.[9–11] However, ultrasound has been shown to be unreliable for visualizing the extent of the thermal ablation zone.[9] Hyperthermic ablation often results in a hyperechoic region due to out-gassing of water vapor formed during the procedure, which is absorbed following the procedure. This hyperechoic region results in the ablation zone being obscured on B-mode images, making B-mode images unreliable for monitoring the extent of thermal ablation. Following the disappearance of the hyperechoic focus, the ablation zone typically manifests as a zone of mixed echogenecity on B-mode images. Delineating ablation zone boundaries in follow-up is also difficult with ultrasound, as the ablation zone in follow-up has been reported to be hyperechoic, hypoechoic, and isoechoic when compared to the surrounding liver parenchyma.[10]

Magnetic resonance (MR) and computed tomography (CT) imaging are also viable candidates for needle guidance and monitoring thermal ablation. MR imaging has several desirable features including good soft tissue contrast and the ability to monitor temperature changes.[12] MRI suffers from the high cost of using MR equipment, poor availability of MR-compatible RF ablation equipment, and limited availability of interventional MR systems. CT imaging can be useful for guidance, especially for tumors located in the hepatic dome where it may not be possible to use ultrasound guidance.[13] CT can also visualize ablation zones, but it cannot be done in real-time and, in general, requires the use of iodinated contrast agents. In addition, CT is more costly than ultrasound imaging and exposes the patient to ionizing radiation.

The coagulation zones resulting from RF ablation are known to be significantly stiffer than the untreated regions, due to protein denaturation and dehydration.[14–18] Due to

these large stiffness changes, ultrasound elastography can provide reliable, high-contrast images for monitoring the size and extent of ablation zones created using electrode-based thermal ablative therapy.[17] Both quasistatic and dynamic approaches have been utilized to monitor the extent of the ablation zone.[19–23] When performing elastographic imaging, it is necessary to apply a stress or mechanical stimuli to the region of interest, which can be difficult for abdominal organs. But following ablation, the RF electrode is strongly bonded to the ablated tissue. Due to this bond, minute displacements may be applied to the RF electrode (on the order of a fraction of a millimeter) in order to generate the necessary deformation for elastographic imaging. This procedure is referred to as electrode displacement elastography.[14,24,25] This method of tissue displacement offers the flexibility of performing elastographic imaging either during or immediately after the RF ablation procedure. It also helps to reduce lateral and elevational motion in surrounding tissue, thereby increasing the quality of the strain images generated. In general, in the presence of an ablated region or mass, the stress distribution due to an applied deformation would not be uniform. The stress distribution generated using electrode displacement elastography has been previously evaluated to determine the contrast and lesion delineation capabilities.[26]

We have previously shown the feasibility of the electrode displacement method using finite element analysis simulations, tissue-mimicking phantom experiments, and *ex vivo* animal experiments.[14,24,25] This paper evaluates the *in vivo* implementation of the electrode displacement technique in exposed, healthy liver tissue during RF ablation procedures in a porcine animal model.

II. MATERIALS AND METHODS

II.A. Porcine animal model

Four female domestic swine were used for this study. The study was approved by the research animal care and use committee of the University of Wisconsin-Madison. Animal husbandry and experimental studies were compliant with the NIH Guide for Care and Use of Laboratory Animals (http://oacu.od.nih.gov/regs/guide/guidex.htm). General anesthesia was induced initially with an intramuscular injection of teletamine and zolazepam (Telazol, Fort Dodge Laboratories, Fort Dodge, IA) and xylazine (Rompun, Bayer Corporation, Shawnee Mission, KS), and maintained with 1%–3% inhaled isoflurane. The anesthetized pigs were placed in a supine position and the liver exposed through a midline incision. Thirteen RF ablations were created in the normal liver parenchyma, and electrode displacement utilized for strain imaging. RF ablations were performed in all four lobes of the liver. The only criterion for the selection was whether the thickness of the lobe could support the formation of an ablation zone, leaving ∼1−3 cm of normal tissue from the liver surface to the ablated region.

RF ablation procedures were performed using a Cooltip™ RF ablation system (Valleylab, Boulder, CO). The RF electrodes were 17 gauge (1.5 mm) in diameter with a 3.0 cm exposed tip. Ablation zones were created by applying power

for 10 min per ablation using the impedance-controlled power pulsing algorithm. This duration was chosen since it provides a sufficient ablation zone size for ultrasound B-mode and strain imaging within the transducer field of view. After the ablation procedures, electrode displacement elastography was performed on the thermal ablations. Radiofrequency data were acquired within 10–15 min of the end of the ablation procedure, for all the ablated regions.

II.B. *In vivo* electrode displacement strain imaging

The ultrasound system utilized to guide ablation applicator placement was a Siemens Antares (Siemens Medical Solutions, USA Inc., Issaquah, WA) real-time scanner equipped with a 10 MHz center frequency linear-array transducer (VFX 13–5) with a bandwidth of approximately 60%. After the ablation procedure, the scanner was also used to collect RF data for electrode displacement elastography. Loops of RF echo signal data were collected during freehand perturbation of the ablation electrode. Pairs of these RF data frames were analyzed using a 2D multistep method for displacement estimation, followed by a linear least-squares strain computation algorithm.[27] Following electrode displacement-based strain imaging, the liver was excised and the ablation zone exposed for gross-pathology measurements by slicing along the ultrasound and elastographic imaging plane using a commercially available meat slicer.

II.C. Pathological correlation

Areas measured on gross-pathology images of the ultrasound scan plane were compared with areas measured on strain images generated for the 13 separate ablation zones. The area measurements were performed without any registration performed between the pathology and strain images. The segmentation of the strain images was performed by three of the authors of this paper using a polygon fitting tool from IMAGEJ (public domain software developed at the NIH) for segmentation. Two of the authors performing the segmentations had less than one year of experience working in the field of strain imaging, while the third author performing segmentations had multiple years of experience working in the field of elastography. Since the strain imaging results are high-contrast images, visualization of the ablation zone on the strain images is not difficult. All three authors' roles in the field of elastography were that of graduate researchers in Medical Physics and Engineering disciplines. The observers [A (NR), B (RD), and C (SB)] were blinded to both the ultrasound B-mode and pathology image prior to lesion segmentation on the strain images of the thermal ablation zones, which were also randomized for each observer. The only guidance provided to the observers was to delineate the stiffer or darker region on the strain image from the surrounding softer or lighter background liver tissue. Segmentation by each observer resulted in the creation of a mask image, where the pixels belonging to the thermal ablation zone were identified. The observers were also asked to segment the ablation zones from corresponding randomized

TABLE I. Regression coefficient and equations of the linear fit to the data.

Observer	r	Linear fit
A	0.824	$y=0.67x+0.876$
B	0.901	$y=1.78x-1.17$
C	0.465	$y=0.59x+0.67$
Mean	0.894	$y=1.23x-0.42$

B-mode images after segmenting the strain images. The area of the thermal ablation in the strain image was then calculated as the sum of the areas of all the pixels identified as belonging to the thermal ablation zone.

The strain images were also segmented using an automated segmentation algorithm developed in our laboratory. These automated segmentations were also compared to pathology measurements using linear regression. The segmentation algorithm consisted of a series of basic morphological image processing steps, such as dilation and opening.[28] First, a 3×3 pixel averaging filter was applied to smooth the image. A binary image was created by thresholding at a value adjusted for the amount of strain present in the image. Next, a mask was created that removed all "holes" in image objects through a process of iterative dilation and masking with the background. Morphological opening was performed with a disk structural element with radius 30% of the size of the largest object in the image, where size is defined to be the radius of the largest circle that would fit inside objects in the image. The opening was performed to isolate large, nearly convex masses. The ablation zone was assumed to be the mass lying near the center of the image, isolated through iterative dilation and masking. Dilation with a structural element 50% the size of the opening structural element and masking with the original threshold image restored the outer mass of the ablation zone. Finally, morphological closing with a structural element 65% of the opening structural element's size ensured a realistic shape. For two thermal ablations, it was necessary to replace the needle artifact using uniformly distributed random numbers corresponding to strains between 0% and 0.2% in order to achieve proper automated segmentation.[29]

In the gross-pathology photographs of the corresponding ultrasound imaging plane (marked on the liver surface), the extent of the ablation zone was delineated manually, based on the transition between white and pink tissue regions. The ultrasound scan plane was identified by marking the position of the linear-array transducer on the liver surface. This mark recorded the orientation of the transducer relative to the ablation electrode; the needle track from the RF ablation was used to obtain the imaging plane for pathology measurements. No fiducial markers were introduced into the scan plane so comparison of the elastographic segmentations to the pathology were made manually based on the shape of the region depicted. Representative (a) ultrasound B-mode, (b) displacement, (c) axial-strain, and (d) gross-pathology photographs of the ablation zone are illustrated in Figs. 1 and 2, respectively. A linear fit was performed between gross-
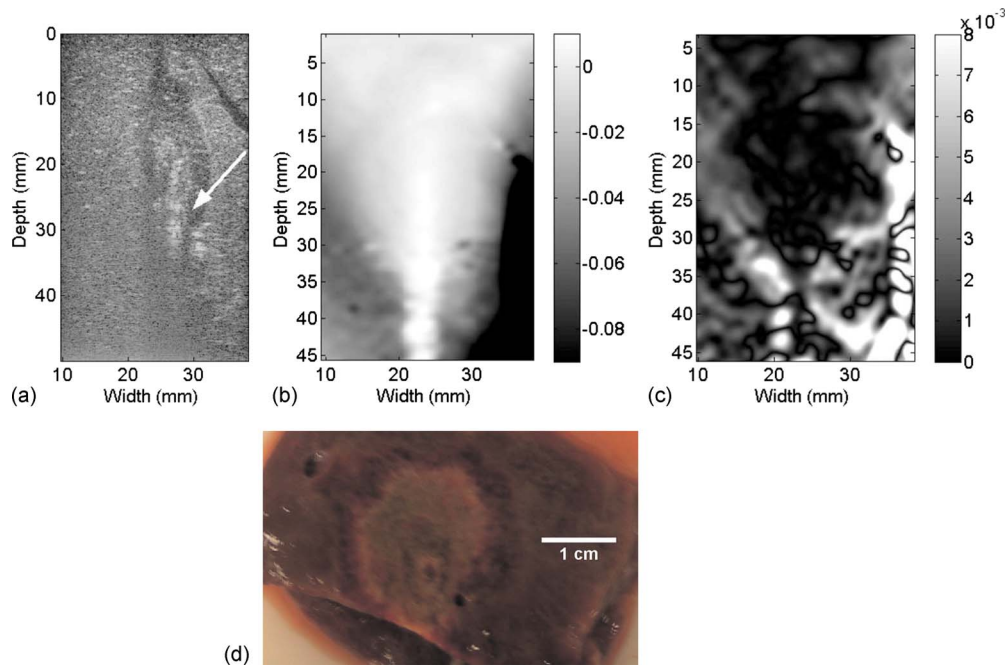
FIG. 1. Representative images of an RF ablated region, comprising (a) the ultrasound B-mode image, where the needle track is identified by the white arrow; (b) the local displacement image, where the displacements plotted are in mm, and the corresponding (c) axial-strain; and (d) gross-pathology image. Note the irregular ablation zone shape in the strain image.
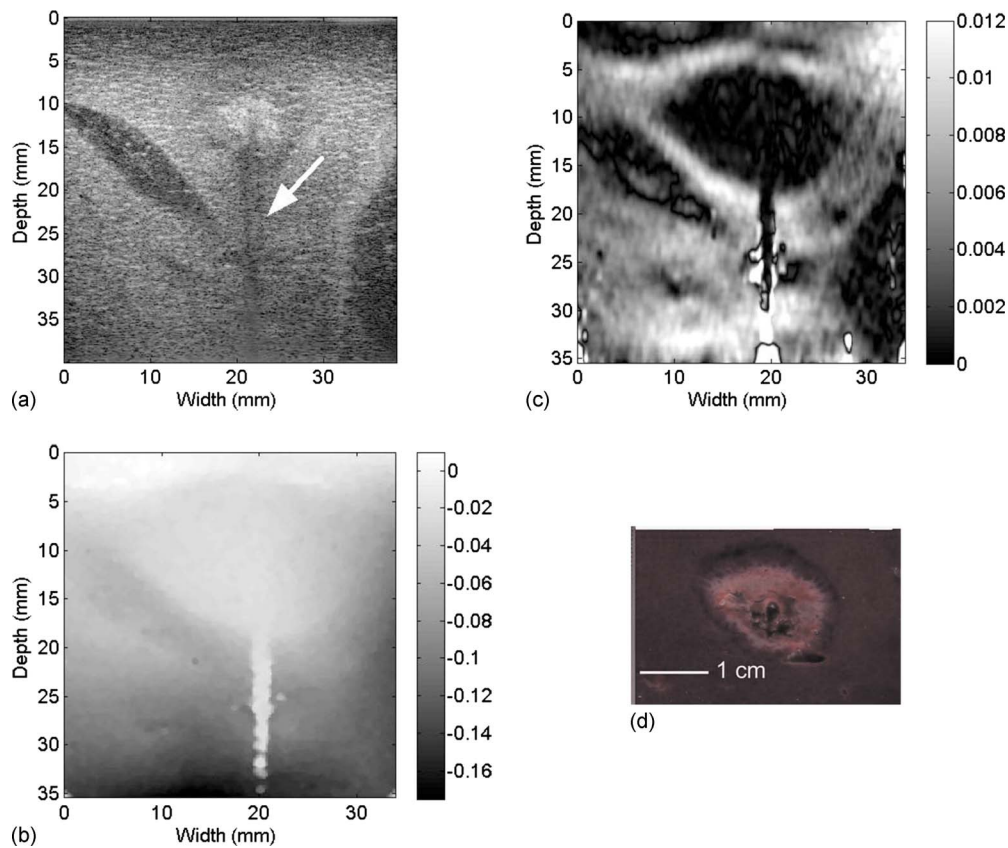

FIG. 2. Image of an RF ablated region with an approximately ellipsoidal shape. Similar to Fig. 1, the (a) ultrasound B-mode image, where the needle track is identified by the white arrow is shown; (b) the local displacement image, where the displacements plotted are in mm, and the corresponding (c) axial-strain; and (d) gross-pathology image.
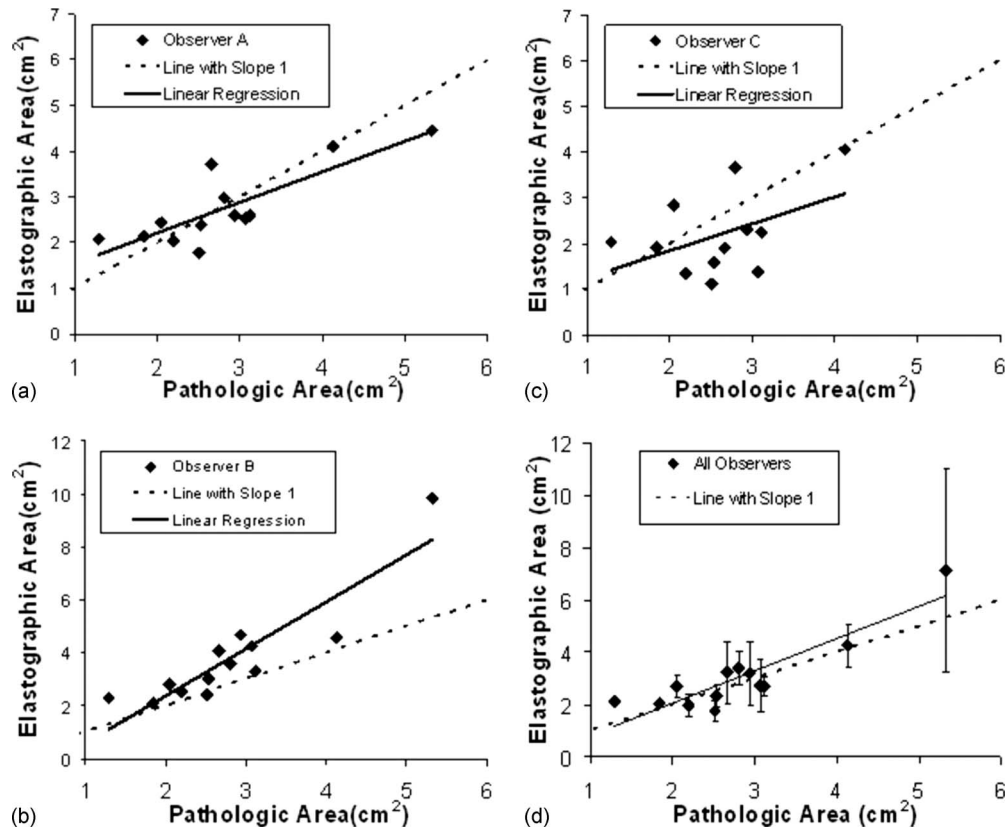
FIG. 3. Comparison of the areas of thermal ablation zones between strain images, manually segmented by three observers and gross-pathology images. A linear fit using the area estimated from the gross-pathology photographs was performed for each observer [A (NR), B (RD), and C (SB)]. (d) The area measurements were also averaged, and the linear fit performed. The dashed line indicates a line with slope of 1, or measurements when an exact match between areas measured on pathology and strain images are obtained. Error bars in (d) indicate one standard deviation of the area measurements estimated by the observers.

pathology and elastographic area measurements for each individual observer and the results are presented in Table I and Fig. 3. A linear fit was also performed between the mean values of the strain measurements of the three observers to determine the correlation between the two measurements. In one of the cases, an observer was unable to delineate ablation zone boundaries in the strain images. For this case only the values from two observers were averaged. In addition, discrepancies in boundary delineation were also evaluated based on the differences between the gross-pathology boundary and boundary segmented by the observers, with the mean and standard deviation presented in Table II. These measurements were made after aligning the centroids of the pathology and observer segmentations, and accounting for ablation zone shape. The differences between a straight line passing through this common centroid and the two boundaries at 36 locations were estimated to compute the boundary discrepancy. The results depict the possible errors with the visualization of the each of the ablation zones for all three observers and for the automated segmentation results in Table II.

III. RESULTS AND INTERPRETATION

III.A. Pathological correlation

In this paper, cross-sectional areas were determined according to image segmentation and no attempt was made to

perform principal axis measurements for pathological correlation. This is justifiable due to the highly irregular geometries demonstrated in the strain images. The ablation depicted by the strain image in Fig. 1, in particular, demonstrates the irregular nature of the boundaries of an RF ablation. Presented with similar images it would be difficult to consistently define principal axes among different observers. This being the case, no attempt to measure and compare principal axes was performed. However, in some of the RF ablation procedures we do obtain ablation zones that are elliptical as illustrated in Fig. 2.

The results of the correlation between the multireader segmentation and pathology area measurements are summarized in Fig. 3 and Table I. On one of the strain images, one observer was unable to identify ablation zone boundaries. In two cases, two of the three observers were unable to delineate ablation zone boundaries on the B-mode images. In one case, where the thermal ablation zone was isoechoic, none of the observers were able to identify ablation zone boundaries on the B-mode image. For the strain images, the correlation coefficient between areas measured on pathology and mean areas measured on strain images was found to be $r = 0.894$ ($p < 0.001$). The error bars shown for each point are equal to one standard deviation of the three or two area measurements, respectively. An attempt to perform a linear regres-

TABLE II. Boundary discrepancies between gross-pathology and the observer and automated segmentations of strain images.

Ablation no.	Observer A (mm)	Observer B (mm)	Observer C (mm)	Automated (mm)
1	1.47 ± 0.80	1.77 ± 0.96	3.50 ± 0.82	2.10 ± 1.30
2	1.58 ± 0.93	1.84 ± 0.97	2.22 ± 1.33	2.61 ± 1.19
3	1.47 ± 0.76	0.93 ± 0.66	3.13 ± 1.09	1.58 ± 0.79
4	4.31 ± 1.44	2.91 ± 1.44	4.64 ± 2.12	2.93 ± 1.44
5	2.39 ± 0.004	2.67 ± 0.007	6.08 ± 1.56	2.94 ± 0.01
6	2.72 ± 0.056	5.31 ± 1.25	NA	5.31 ± 1.25
7	1.58 ± 1.24	2.31 ± 1.33	1.19 ± 1.13	2.57 ± 1.54
8	1.13 ± 0.001	0.66 ± 0.001	0.72 ± 0.001	0.98 ± 0.003
9	3.17 ± 0.98	2.12 ± 1.04	4.61 ± 1.20	4.02 ± 0.86
10	2.44 ± 0.07	7.61 ± 0.15	2.03 ± 1.38	2.60 ± 0.06
11	1.23 ± 0.54	1.57 ± 0.59	1.14 ± 0.435	1.46 ± 0.81
12	1.75 ± 0.05	2.02 ± 0.058	2.57 ± 0.33	0.02 ± 0.05
13	3.03 ± 0.57	3.03 ± 0.57	0.59 ± 0.22	10.74 ± 0.06

sion on a plot of gross-pathology areas versus the ultrasound B-mode areas yielded a nearly horizontal line with a slope of 0.29, and a correlation coefficient of $r = 0.33$. There was considerable interobserver variability on the noisier, less obvious strain images. This being the case, a linear regression was performed between elastographic area measurements for each observer and pathology measurements. It was found that two of the three observers showed a fairly high correlation coefficient, while the value for the third observer was considerably lower. As illustrated in Table II, considerable differences between observers exist for measurements on the same ablation zone (Fig. 3).

The results of the automated segmentation shown in Fig. 4, were comparable to the result of segmentation by the human observers, though the automated segmentation performed slightly worse. The reason for this is probably that some of the images were quite noisy, and a human observer was better able to draw realistic boundaries on a noisy image than the automated segmentation routine was able to pro-
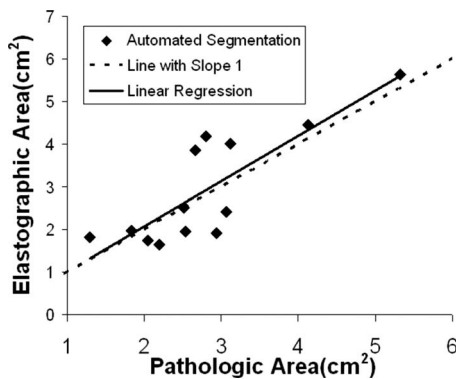

FIG. 4. Comparison of the areas of thermal ablation zones in the marked imaging plane using automated segmentation of strain images. The dashed line indicates a line with slope of 1, or measurements when an exact match between areas measured on pathology and strain images are obtained. The linear regression between the pathology area and the strain area shows a correlation coefficient, $r = 0.828$ ($p < 0.001$).

duce. A linear regression was also performed for the automated segmentation, and the linear fit was found to have a correlation coefficient $r = 0.828$ ($p < 0.001$).

III.B. Blood vessels and strain imaging

An interesting phenomenon worth noting on the strain images produced during this study is presented in Fig. 5. Ultrasound imaging has long been used to image blood vessels, and strain images generated during this study show that strain imaging preserves this functionality. In Fig. 5, the B-mode image of an ablation zone [Fig. 5(a)] illustrates the presence of a blood vessel, possibly above the ablation zone. In the strain image the blood vessel manifests as a bright artifact in the image. The strain image [Fig. 5(c)] confirms the presence of the blood vessel cutting across the ablation zone, where it manifests as a bright decorrelation artifact in the image. The pathology image also shows this blood vessel. For this particular ablation, we were unable to expose the imaging plane when cutting through the ablation zone, and the pathology photograph shows a cross-section of the ablation zone perpendicular to the needle track. In the gross-pathology photograph, the two holes visible on either side of the ablation zone indicate the presence of the blood vessel. Reliably imaging blood vessels during RF ablation is particularly important because blood vessels act as heat sinks during ablation procedures and reduce the efficiency of the procedure.

In addition, the stiffer region in the strain image appears to encompass the entire image. If the entire dark region is assumed to be the thermal ablation zone, this yields a cross-sectional area of approximately 9 cm^2, an unrealistically large value for the ablated area. This is possibly an artifact due to the presence of the blood vessel. It is possible that the displacement of the ablation electrode was not transmitted above the blood vessel leading to reduced or no deformation on the other side of the blood vessel. The displacement image in Fig. 5(c) supports this hypothesis as the displacements on the side of the blood vessel closer to the transducer are very small compared to the local displacement on the other side of the blood vessel. Thus the lower strain values in the image may be attributed to mechanical boundary conditions rather than an underlying modulus contrast, leading to the overestimation of the ablation zone.

IV. DISCUSSION AND CONCLUSION

Previous phantom and *ex vivo* experiments have demonstrated the accuracy of strain imaging for measuring the extent of tissue necrosis following RF ablation.[13,16,24] In the *ex vivo* studies, the correlation between pathology and strain imaging for cross-sectional imaging was found to be as high as 0.9371 ($p < 0.000\,01$) for a sample of 40 thermal ablation zones. In this study, electrode displacement elastography was performed *in vivo* on normal porcine liver parenchyma after RF ablation to create the thermally coagulated regions. A smaller sample size of 13 ablation zones was used and three human observers manually segmented the ablation zones obtained from strain images. A linear regression between elas-
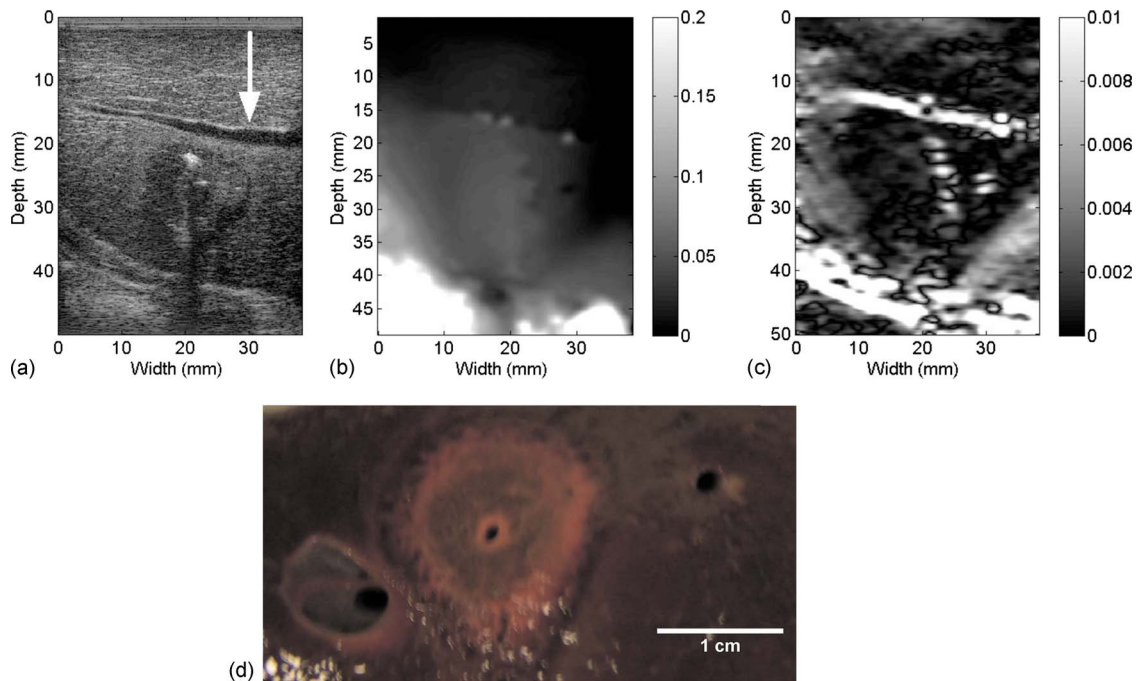
FIG. 5. Images illustrating an interesting case with an RF ablation procedure. The location of the blood vessel is indicated by the arrow in (a) the ultrasound B-mode image. (b) The corresponding local displacement image where the units for displacement estimated are in mm, (c) electrode displacement strain image, and the (d) gross-pathology image are also shown. Notice the presence of a blood vessel which manifests itself as a bright decorrelation streak through the ablation zone in the strain image.

tographic and pathologic areas yielded a correlation coefficient of 0.894 ($p < 0.0001$). For the case of automated segmentation, a linear regression between elastographic and pathologic area measurements yielded a correlation coefficient of 0.828 ($p < 0.001$).

The strain images illustrated in this paper indicate that thermally ablated liver tissue may be differentiated from healthy liver parenchyma using an *in vivo* animal model. Comparison of the ablated areas between gross-pathology and strain images was performed using boundary contour delineation, which results in reasonably good agreement between strain and gross-pathology measurements. This was shown for the case with multiple human observers and using automated segmentation based on morphological operators. The automated segmentation algorithm can be improved or augmented using manual interventions to improve the segmentation performance. Although several of the segmentations show good agreement, some of the manual segmentations presented in Table II show considerable interobserver variability. This is probably due to the alignment of the ultrasound imaging plane to the 2D slice utilized for the gross-pathology measurements. As previously mentioned, no fiducial markers were introduced into the scan plan to indicate the exact plane for gross-pathology measurements. Coregistration was performed based on the shape of the respective gross-pathology and strain contours for the scan plane identified based on a line burned onto the liver parenchyma after the ablation procedure. Clinicians generally treat a normal tissue margin of approximately 1 cm beyond the tumor boundary to ensure that the entire tumor has been treated. Results reported in the literature indicate that an ablative margin of at least 5 mm or larger is necessary to reduce local tumor recurrence.[30] Note that the boundary discrepancies shown in Table II are still less than the 5 mm safety margin. We anticipate that with accurate registration the boundary discrepancies between strain imaging and gross-pathology would be minimized further. These results also demonstrate the need for 3D strain imaging for complete tracking and measurement of the lesion volume.[29] Volume imaging of the ablation zone will reduce errors associated with area measurements.[29]

The other limitations of this study include the use of a high transducer center frequency, which is not feasible for imaging human patients during a percutaneous procedure. Ultrasound imaging was performed using an open-chest preparation with the transducer placed directly on the liver surface. This study, therefore, does not evaluate the impact of attenuation introduced by overlying tissue encountered with percutaneous procedures. The mechanical boundary conditions also impact the information depicted on the strain image. Note that the quality of the strain images presented in this paper can be significantly improved with the implementation of the strain estimation algorithm in real-time to enable assessment of the mechanical boundary conditions and the corresponding impact on the strain images during data acquisition.

Future works will assess the viability of this technique in more realistic percutaneous animal models, using 3D volume imaging[29] along with improved registration between pathological and imaging planes. Tumor models in animals will also be used to evaluate the ability of electrode displacement elastography to delineate and differentiate the volume treated

from the volume to be treated. If successful, these results would enable the use of this technology for clinical applications.

ACKNOWLEDGMENTS

[a] Author to whom correspondence should be addressed. Electronic mail: tvarghese@wisc.edu; Telephone: (608)-265-8797; Fax: (608)-262-2413.

[1] A. Jemal, R. Siegel, E. Ward, Y. Hao, J. Xu, T. Murray, and M. J. Thun, "Cancer statistics, 008," Ca-Cancer J. Clin. **58**, 71–96 (2008).

[2] Y. Ku, T. Iwasaki, M. Tominaga, T. Fukumoto, T. Takahashi, M. Kido, S. Ogata, M. Takahashi, Y. Kuroda, and S. Matsumoto, "Reductive surgery plus percutaneous isolated hepatic perfusion for multiple advanced hepatocellular carcinoma," Ann. Surg. **239**, 53–60 (2004).

[3] P. Liang and Y. Wang, "Microwave ablation of hepatocellular carcinoma," Oncology **72**, 124–131 (2007).

[4] T. J. Vogl, K. Eichler, R. Straub, K. Engelmann, S. Zangos, D. Woitaschek, M. Böttger, and M. G. Mack, "Laser-induced thermotherapy of malignant liver tumors: General principals, equipment (s), procedure (s)—Side effects, complications and results," Eur. J. Ultrasound **13**, 117–127 (2001).

[5] T. Mala, "Cryoablation of liver tumours—A review of mechanisms, techniques and clinical outcome," Minimally Invasive Ther. Allied Technol. **15**, 9–17 (2006).

[6] S. A. Sapareto and W. C. Dewey, "Thermal dose determination in cancer therapy," Int. J. Radiat. Oncol., Biol., Phys. **10**, 787–800 (1984).

[7] S. N. Goldberg, G. S. Gazelle, and P. R. Mueller, "Thermal ablation therapy for focal malignancy a unified approach to underlying principles, techniques, and diagnostic imaging guidance," AJR, Am. J. Roentgenol. **174**, 323–331 (2000).

[8] R. Lencioni and L. Crocetti, "Image-guided thermal ablation of hepatocellular carcinoma," Crit. Rev. Oncol. Hematol. **66**, 200–207 (2008).

[9] L. Solbiati, S. N. Goldberg, T. Ierace, T. Livraghi, F. Meloni, M. Dellanoce, S. Sironi, and G. S. Gazelle, "Hepatic metastases: Percutaneous radio-frequency ablation with cooled-tip electrodes," Radiology **205**, 367–373 (1997).

[10] L. Solbiati, T. Ierace, S. N. Goldberg, S. Sironi, T. Livraghi, R. Fiocca, G. Servadio, G. Rizzatto, P. R. Mueller, and A. Del Maschio, "Percutaneous US-guided radio-frequency tissue ablation of liver metastases: Treatment and follow-up in 16 patients," Radiology **202**, 195–203 (1997).

[11] L. Solbiati, T. Ierace, M. Tonolini, V. Osti, and L. Cova, "Radiofrequency thermal ablation of hepatic metastases," Eur. J. Ultrasound **13**, 149–158 (2001).

[12] B. D. de Senneville, C. Mougenot, B. Quesson, I. Dragonu, N. Grenier, and C. T. W. Moonen, "MR thermometry for monitoring tumor ablation," Eur. Radiol. **17**, 2401–2410 (2007).

[13] B. J. Park, J. H. Byun, Y. H. Jin, H. J. Won, Y. M. Shin, K. W. Kim, S. J. Park, and P. N. Kim, "CT-guided radiofrequency ablation for hepatocellular carcinomas that were undetectable at US: Therapeutic effectiveness

and safety," J. Vasc. Interv. Radiol. **20**, 490–499 (2009).

[14] T. Varghese, J. A. Zagzebski, and F. T. Lee, Jr., "Elastographic imaging of thermal lesions in the liver in vivo following radiofrequency ablation: Preliminary results," Ultrasound Med. Biol. **28**, 1467–1473 (2002).

[15] T. Wu, J. P. Felmlee, J. F. Greenleaf, S. J. Riederer, and R. L. Ehman, "Assessment of thermal tissue ablation with MR elastography," Magn. Reson. Med. **45**, 80–87 (2001).

[16] R. Righetti, F. Kallel, R. J. Stafford, R. E. Price, T. A. Krouskop, J. D. Hazle, and J. Ophir, "Elastographic characterization of HIFU-induced lesions in canine livers," Ultrasound Med. Biol. **25**, 1099–1113 (1999).

[17] T. Varghese, U. Techavipoo, W. Liu, J. A. Zagzebski, Q. Chen, G. Frank, and F. T. Lee, "Elastographic measurement of the area and volume of thermal lesions resulting from radiofrequency ablation: Pathologic correlation," AJR, Am. J. Roentgenol. **181**, 701–707 (2003).

[18] F. Wu, W. Z. Chen, J. Bai, J. Z. Zou, Z. L. Wang, H. Zhu, and Z. B. Wang, "Pathological changes in human malignant carcinoma treated with high-intensity focused ultrasound," Ultrasound Med. Biol. **27**, 1099–1106 (2001).

[19] M. Zhang, B. Castaneda, J. Christensen, W. Saad, K. Bylund, K. Hoyt, J. G. Strang, D. J. Rubens, and K. J. Parker, "Real-time sonoelastography of hepatic thermal lesions in a swine model," Med. Phys. **35**, 4132–4141 (2008).

[20] O. Kolokythas, T. Gauthier, A. T. Fernandez, H. Xie, B. A. Timm, C. Cuevas, M. K. Dighe, L. M. Mitsumori, M. F. Bruce, and D. A. Herzka, "Ultrasound-based elastography: A novel approach to assess radio frequency ablation of liver masses performed with expandable ablation probes: A feasibility study," J. Ultrasound Med. **27**, 935–946 (2008).

[21] B. J. Fahey, R. C. Nelson, S. J. Hsu, D. P. Bradway, D. M. Dumont, and G. E. Trahey, "In vivo guidance and assessment of liver radio-frequency ablation with acoustic radiation force elastography," Ultrasound Med. Biol. **34**, 1590–1603 (2008).

[22] B. J. Fahey, K. R. Nightingale, S. A. McAleavey, M. L. Palmeri, P. D. Wolf, and G. E. Trahey, "Acoustic radiation force impulse imaging of myocardial radiofrequency ablation: Initial in vivo results," IEEE Trans. Ultrason. Ferroelectr. Freq. Control **52**, 631–641 (2005).

[23] K. Hoyt, B. Castaneda, and K. J. Parker, "Two-dimensional sonoelastographic shear velocity imaging," Ultrasound Med. Biol. **34**, 276–288 (2008).

[24] S. Bharat, T. Varghese, E. L. Madsen, and J. A. Zagzebski, "Radiofrequency ablation electrode displacement elastography: A phantom study," Med. Phys. **35**, 2432–2442 (2008).

[25] J. Jiang, T. Varghese, Q. Chen, T. J. Hall, and J. A. Zagzebski, "Finite element analysis of tissue deformation with a radiofrequency ablation electrode for strain imaging," IEEE Trans. Ultrason. Ferroelectr. Freq. Control **54**, 281–289 (2007).

[26] S. Bharat and T. Varghese, "Contrast-transfer improvement for electrode displacement elastography," Phys. Med. Biol. **51**, 6403–6418 (2006).

[27] H. Shi and T. Varghese, "Two-dimensional multi-level strain estimation for discontinuous tissue," Phys. Med. Biol. **52**, 389–401 (2007).

[28] R. C. Gonzalez and R. E. Woods, *Digital Image Processing*, 2nd ed. (Prentice Hall, Upper Saddle River, 2002).

[29] S. Bharat, T. G. Fisher, T. Varghese, T. J. Hall, J. Jiang, E. L. Madsen, J. A. Zagzebski, and F. T. Lee, "Three-dimensional electrode displacement elastography using the Siemens C7F2 fourSight four-dimensional ultrasound transducer," Ultrasound Med. Biol. **34**, 1307–1316 (2008).

[30] T. Nakazawa, S. Kokubu, A. Shibuya, K. Ono, M. Watanabe, H. Hidaka, T. Tsuchihashi, and K. Saigenji, "Radiofrequency ablation of hepatocellular carcinoma: Correlation between local tumor progression after ablation and ablative margin," AJR, Am. J. Roentgenol. **188**, 480–488 (2007).